ADVANCED ENERGY MATERIALS
www.advenergymat.de

How Does the Creep Stress Regulate Void Formation at the Lithium-Solid Electrolyte Interface during Stripping?

Hanghang Yan, Karnpiwat Tantratian, Kevin Ellwood, Elisa T. Harrison, Mark Nichols, Xiangyang Cui, and Lei Chen**

Interfacial instability from void formation at the solid–solid interface is one of the crucial challenges in solid-state batteries. However, the fundamental mechanism as to how stress is generated in lithium and thus impacts void formation has not been established. A general creep/contact electro-chemo-mechanical model is herein developed to reveal the mechanisms of void formation at the Li/solid electrolyte (SE) interface during stripping. Li stress calculation is achieved by presuming that the strain-rate-dependent creep deformation of Li metal acts like that of an incompressible viscous fluid flow. The results demonstrate that the dominant mechanism that impedes void formation is the creep-induced flux enhancement of vacancies, which are transported into Li metal for a non-ideal Li/SE interface with pre-existing interfacial defects. This contrasts with previous simulations on an ideal flat Li/SE interface in which the vacancy diffusion away from the interface is shown to govern whether voids are formed.

1. Introduction

Solid-state lithium (Li) metal batteries (SSBs), which consist of a solid electrolyte (SE) paired with a Li metal anode, have the potential to offer a superior gravimetric energy density when compared to conventional Li-ion batteries.[1,2] In principle, the impressive high elastic modulus of the SE is enough to physically block the growth of Li dendrites, which currently limits the utilization of a Li metal anode.[3,4] Unfortunately, Li dendrites are unexpectedly observed to nucleate at interfacial voids and cracks between the Li metal and the SE (such as $Li_7La_3Zr_2O_{12}$, LLZO, and Li phosphorus oxynitride, LiPON), and eventually penetrate the SE.[5–7] Another critical problem is the interfacial instability arising from the contact loss at the Li/SE interface during stripping, which lowers the battery's cyclability and ultimately causes cell failure.[8–12] Thus, the dynamic behavior of the mechanical contact at the Li/SE interface needs to be understood to design a better battery cell.

A challenge to maintain mechanical contact at the Li/SE interface is void formation.[13–16] Void formation leads to interfacial porosity, surface roughness, and consequently contact loss.[17–19] Recently, experimental characterization has shown that the stack pressure is an important factor in preventing void formation during stripping in SSBs.[18,20,21] It has been proposed that the pressure-driven creep deformation of Li metal replenishes the void at the Li/SE interface.[18,22] However, void formation at the solid–solid interface involves stress, contact, reaction, and Li/Li^+ transport, which are challenging to observe and measure experimentally. Therefore, the understanding of contact issues during stripping is still in its infancy. Specifically, the fundamental questions as to how the external pressure and current as well as intrinsic material properties impact the internal void formation at the Li/SE interface are unanswered.

Taking a deeper insight into the mechanism of interfacial void formation, when applying current density and stack pressure, the stripping current removes electrons from Li metal and releases Li^+ into the SE to migrate away from the interface (i.e., the flux of Li^+ migration away from the interface, $\mathbf{J}_{migration}$). This generates a large number of vacancies in Li metal near the interface. The flux of the vacancies contributed by the Li metal creep, $\mathbf{J}_{creep}$, and diffusion, $\mathbf{J}_{diffusion}$, can transport the vacancies away from the interface and towards the bulk Li metal, as illustrated in **Figure 1**a. Recent kinetic Monte Carlo (KMC) simulations[23] show that for an ideal flat Li/SE interface, $\mathbf{J}_{diffusion}$ is high enough to transport the vacancies away from the interface and maintain a smooth Li/Li_2O surface even without the stack pressure (i.e., $J_{diffusion} > J_{migration}$ where $J_{\#}$ represents the magnitude of the flux), as illustrated in Figure 1b. However, such an ideal flat interface is unlikely due to the limitation of the experimental conditions and techniques, and pre-existing interfacial defects such as

H. Yan, X. Cui
State Key Laboratory of Advanced Design and Manufacturing for Vehicle Body
Hunan University
Changsha 410082, P. R. China
E-mail: cuixy@hnu.edu.cn

K. Tantratian, L. Chen
Department of Mechanical Engineering
University of Michigan-Dearborn
Dearborn, MI 48128-1491, USA
E-mail: leichn@umich.edu

K. Ellwood, E. T. Harrison, M. Nichols
Research and Innovation Center
Ford Motor Company
Dearborn, MI 48121, USA

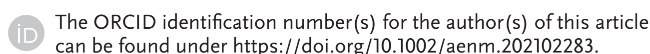
The ORCID identification number(s) for the author(s) of this article can be found under https://doi.org/10.1002/aenm.202102283.

DOI: 10.1002/aenm.202102283

 © 2021 Wiley-VCH GmbH

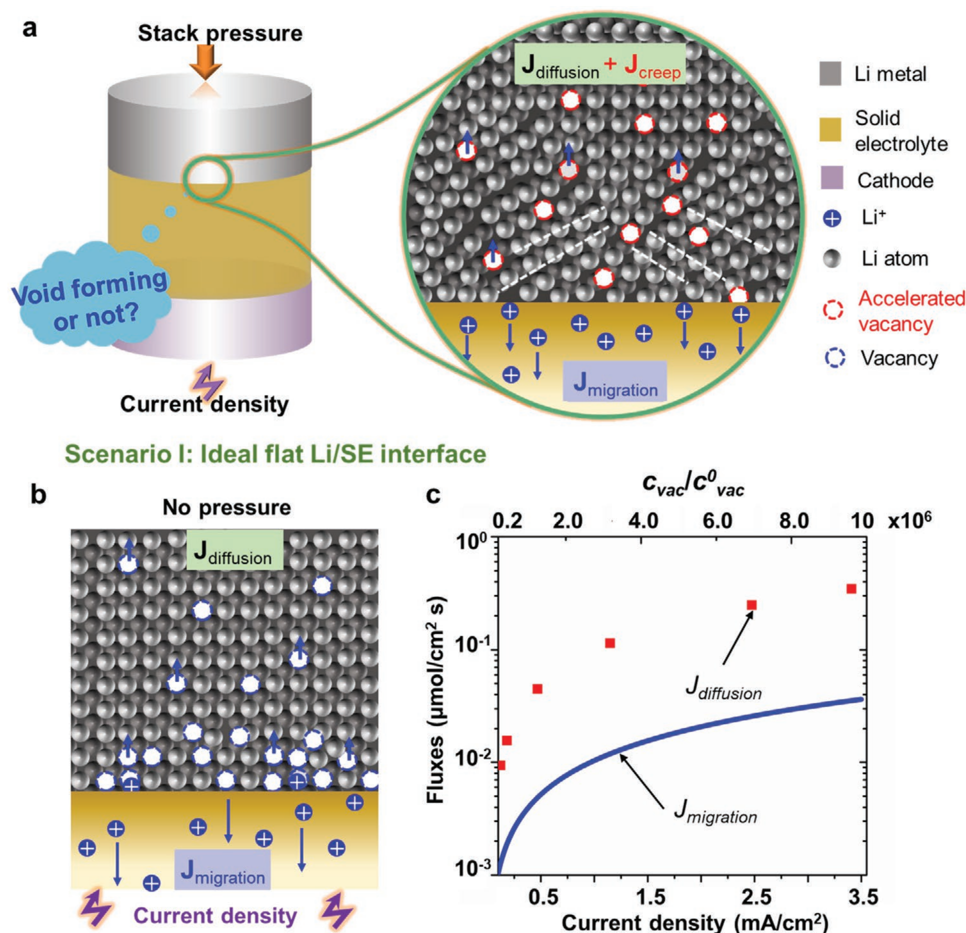

Figure 1. Scenario I: an ideal flat Li/SE interface. a) Schematic illustration of three fluxes that are presented during the void formation at the interface: $\mathbf{J}_{\text{migration}}$, $\mathbf{J}_{\text{diffusion}}$, and $\mathbf{J}_{\text{creep}}$. b) Schematic illustration of the competing influence on the void formation induced by $\mathbf{J}_{\text{migration}}$ and $\mathbf{J}_{\text{diffusion}}$ at the ideal flat Li/SE interface. c) The comparison between the quantities of $J_{\text{migration}}$ and $J_{\text{diffusion}}$.

pores/voids are common on the SE surface.[7,24] Some experimental measurements show that pre-existing defects often grow, particularly under conditions of no or small stack pressure, which contrasts with the KMC simulations.[17,18,22] Therefore, it is reasonable to speculate that $\mathbf{J}_{\text{diffusion}}$ cannot impede the void formation for a non-ideal Li/SE interface with pre-existing defects, as illustrated in **Figure 2**a. However, the mechanism as to how the non-ideal Li/SE interface modulates $\mathbf{J}_{\text{diffusion}}$ is still unclear. On the other hand, a sufficiently high stack pressure is experimentally found to impede the formation of voids.[17,18] It is thus hypothesized that the creep-induced flux of vacancies, $\mathbf{J}_{\text{creep}}$, rather than $\mathbf{J}_{\text{diffusion}}$, is the dominant factor that impedes void formation. To be more specific, $\mathbf{J}_{\text{creep}}$ is fast enough to move away from the new vacant sites ($J_{\text{creep}} > J_{\text{migration}}$) if a sufficiently high stack pressure is applied, as illustrated in Figure 2b. From the atomic perspective, the creep deformation of Li metal is accompanied by dislocations, which can reduce the diffusion barrier of vacancies.[25,26] However, the knowledge as to how the local/microscopic interfacial Li stress arises due to the macroscopic stack pressure and internal electrochemical reaction, as well as how Li stress impacts $\mathbf{J}_{\text{creep}}$, remain little explored. An in-depth understanding of the above knowledge gaps is urgent.

One important aspect is that the mechanical stress manifests more acutely at the solid–solid interface. Several experimental and theoretical works attempt to illustrate how the Li stress is generated and transmitted when the Li metal is in contact with the SE; however, the measured and calculated Li stress differs significantly from one research work to another.[27–31] This complex mechanical interaction at the interface has not yet been clarified. Recent experimental observations reveal that Li metal exhibits a strain-rate-dependent creep behavior dominated by dislocation climb over a wide range of battery-charging/discharging conditions.[32,33] Thus, the creep mechanism needs to be correlated with the stack pressure and current density during charging/discharging to fully understand the electro-chemo-mechanical interaction behaviors between Li metal and the SE. Herein, we postulate that Li metal behaves like an incompressible viscous fluid via a creep deformation mechanism under compression, where the hardness of Li metal (≈MPa)[34] is much smaller than that of the SE (≈GPa)[35] at the microscale. Therefore, the fluid-structure interaction (FSI) theory can be introduced to predict the Li stress generated.

In this work, we aim to systematically decipher the mechanisms of the void formation at the Li/SE interface during stripping by using a newly developed creep/contact electro-chemo-mechanical

© 2021 Wiley-VCH GmbH

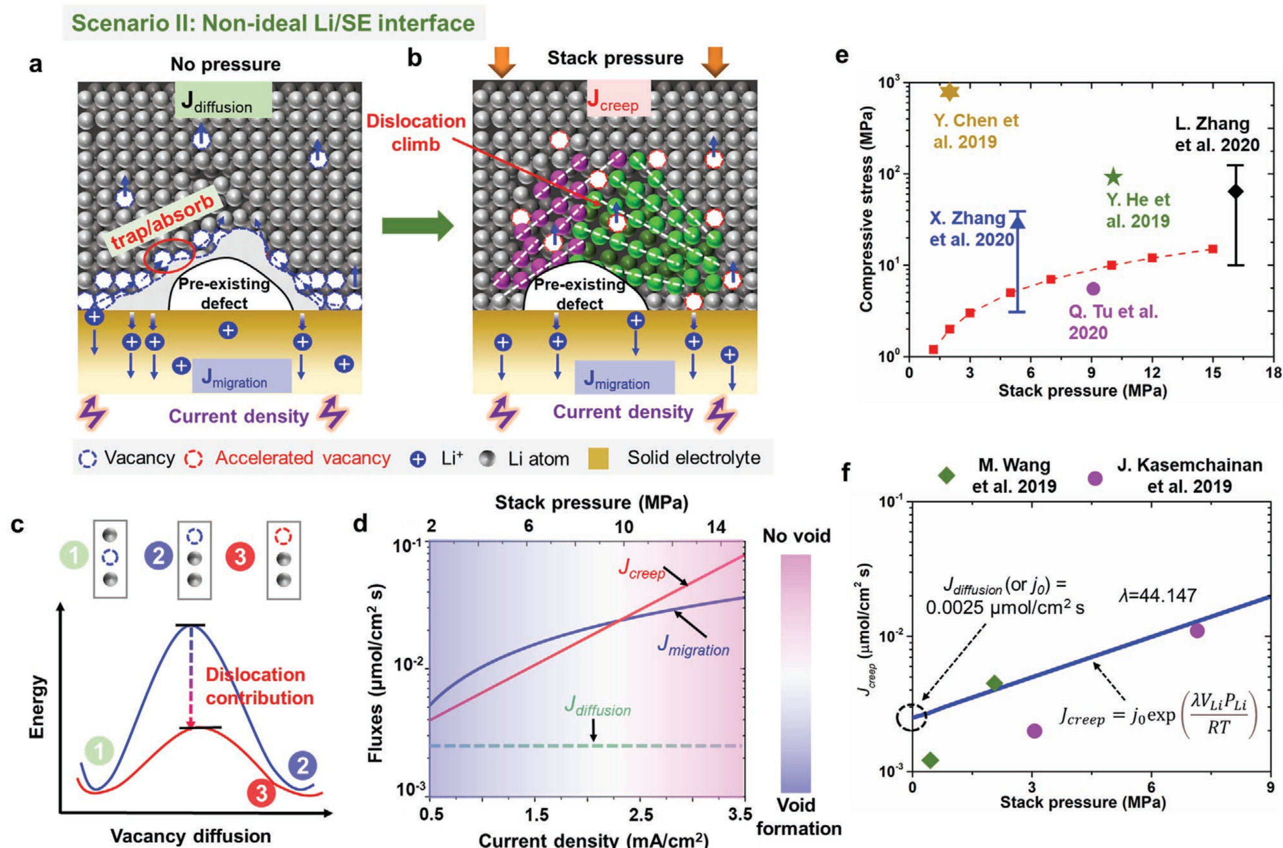

Figure 2. Scenario II: a non-ideal Li/SE interface with pre-existing defects. a) A smaller $J_{diffusion}$ is presented due to the vacancy trapped/absorbed at the surface of pre-existing defects, leading to $J_{migration} > J_{diffusion}$ which is not fast enough to transport the interfacial vacancies into the bulk Li metal and the void is formed. b) If applying a sufficiently high stack pressure, J_{creep} is higher than $J_{migration}$; therefore, the vacancies are transported away from the interface and into the bulk Li metal and the void formation is impeded. c) The plot of the energy barrier against the diffusion coordinate for the vacancy diffusion under the contribution of the dislocation induced by the stack pressure. d) The comparison between the quantity of $J_{migration}$, J_{creep}, and $J_{diffusion}$. e) The calculated compressive stress at Li/SE interface as the function of stack pressure, at the current density of 0.5 mA cm^{-2} (red square) together with the reported interfacial compressive stress in literatures, Chen et al.[28] (yellow hexagon), Zhang et al.[31] (blue triangle), Tu et al.[29] (pink circle), He et al.[30] (green star) and Zhang et al.[27] (black rhombus). f) The plot of the calibrated J_{creep} as a function of stack pressure (blue) together with the reported J_{creep} in literatures, Wang et al.[22] (green rhombus) and Kasemchainan et al.[18] (pink circle).

model. The creep stress distribution of Li metal is calculated by introducing a novel FSI theory where the strain-rate-dependent creep deformation behavior of Li metal is analogous to an incompressible viscous fluid flow. LLZO is chosen as the SE for demonstration. To clarify the effect of $J_{diffusion}$ on void formation, a 1D model with the ideal flat Li/SE interface is first investigated. For the non-ideal Li/SE interface, the effect of pre-existing interfacial defect features (e.g., pore length and pore depth) on the void formation behavior is comprehensively investigated. To determine the preferred stack pressure that could impede void formation under different requirements, the competing influences between stack pressure and current density on the void formation are intensively explored, which yield a map of void formation that can inform whether the stack pressure sufficiently impedes void formation. Lastly, to clarify the effect of the material properties on interfacial mechanical stability, high-throughput simulations yield an interfacial mechanical stability window as a function of ionic conductivity and exchange current density which can give quantitative information on whether the fabricated SE can maintain a stable interface.

2. Results and Discussion

2.1. Ideal Flat Li/SE Interface

We first investigate a scenario in which the ideal flat Li/SE interface is considered. When applying a current density without stack pressure, $J_{migration}$ removes Li^+ from the interface, generating a large number of vacancies in Li metal near the Li/SE interface. Thus, the higher the stripping current density, the larger the concentration of the Li^+ removed from the interface, and thus the larger the concentration of vacancies is generated. Such a concentration of vacancies at the interface could produce a high vacancy diffusion gradient (i.e., $J_{diffusion}$) which can quickly transport vacancies away from the interface, thus, void formation is impeded as illustrated in Figure 1b.

To clarify the void formation mechanism for the scenario of the ideal flat Li/SE interface, a quantitative analysis and comparison between $J_{migration}$ and $J_{diffusion}$ are introduced. Recent experiments show that the ionic transference number of LLZO is near unity,[36] and thus it can be assumed that all of the

© 2021 Wiley-VCH GmbH

current density in the Li/LLZO interface is generated by the flux of Li^+. With a specific applied current density, $\mathbf{J}_{migration}$ can be described as:

$$\mathbf{J}_{migration} = \frac{\mathbf{i}_{interface}}{z_+ F} \tag{1}$$

where $\mathbf{i}_{interface}$ is the interfacial current density, F is Faraday's constant, and z_+ is the valence of cations. For $\mathbf{J}_{diffusion}$, the defect relaxation model developed by Schmalzried and Janek[37] can be used to estimate the magnitude of the limiting flux of the vacancy diffusion:

$$J_{diffusion} = \left(1 - \frac{c_{vac}}{c^0_{vac}}\right) c^0_{vac} \sqrt{\frac{D_{vac}}{\tau_{vac}}} \tag{2}$$

where c_{vac} is the maximum value of the concentration of the vacancies at the Li/SE interface which depends on the current density during stripping[38–40] (calculation details can be found in S2 and Figure S3 Supporting Information). c^0_{vac} is the equilibrium concentration of the vacancies, and is approximately 8×10^{-9} mol cm^{-3} estimated by ab initio calculations.[41] D_{vac} is the diffusion coefficient of Li vacancies and is around 10^{-10} cm^2 s^{-1} at room temperature as reported in previous KMC simulations[23] and others.[42–44] τ_{vac} is the relaxation time of Li vacancies, which is assumed to be approximately 5 s.[19]

Figure 1c compares the quantities of $J_{migration}$ and $J_{diffusion}$ for the ideal flat Li/SE interface subjected to a current density from 0.1 to 3.5 mA cm^{-2}, which are commonly used in experiments.[18,38,45] To focus on the effect of $J_{diffusion}$, no stack pressure is applied. It is observed that the calculated $J_{migration}$ is in the range of 0.001 to 0.0363 µmol cm^{-2} s^{-1}, while the calculated $J_{diffusion}$ is in the range of 0.01 to 0.35 µmol cm^{-2} s^{-1} with the normalized maximum vacancy concentration, i.e., from 2.6×10^5 to 9.6×10^6. Obviously, $J_{diffusion}$ is larger than $J_{migration}$ whatever current density is applied, which implies that the vacancies diffuse away fast enough from the interface such that void formation is impeded. Such results are consistent with the observations in previous KMC simulations.[23]

2.2. Non-ideal Li/SE Interface with Pre-existing Defects

2.2.1. Competition Mechanism between J_{creep} and $J_{migration}$ on Void Formation

In this scenario, the non-ideal Li/SE interface with pre-existing defects is modeled. As illustrated in Figure 2a, vacancy diffusion along the surface of the pre-existing defect is faster than it diffuses into the bulk region (terrace-ledge-kink model) due to the lower self-diffusion barriers along the defect surfaces.[19,46] Then, vacancies are trapped/absorbed by the defect[47] and causing the defect (e.g., pore) growth. Therefore, the vacancies at the non-ideal Li/SE interface with defects are reduced when compared to that at the ideal flat Li/SE interface, as observed in Figure S4 (Supporting Information) (detailed simulation procedures can be found in Figure S4, Supporting Information). Therefore, $J_{diffusion}$ is much lower than $J_{migration}$ without stack pressure, as shown in Figure 2d where the $J_{diffusion}$ is calculated as 0.0025 µmol cm^{-2} s^{-1} through the calibration, whose details can be found in Figure S3 (Supporting Information) and Figure 2f. These numbers suggest that as Li^+ is stripped, $J_{diffusion}$ is not fast enough to transport the Li^+ migration generated vacant sites away from the interface, resulting in void formation and eventually contact loss.

When applying a pressure, creep deformation occurs inside the Li metal due to dislocation climb, as illustrated in Figure 2b. From the atomic perspective, the stack pressure-induced dislocation reduces the energy barrier of the vacancy diffusion, leading to fast vacancy transport into the bulk Li metal,[25,26] as shown in Figure 2c. It is easily understood that the higher stack pressure presents a larger dislocation climb, resulting in the higher flux of the vacancies transporting away from the interface and towards the bulk Li metal. In addition, according to recent experimental measurements,[18,22] the critical stack pressure to prevent void formation shows a nonlinear relationship with the current density. Thus, the relationship between the pressure and the $\mathbf{J}_{creep}$ can be expressed as

$$\mathbf{J}_{creep} = j_0 \exp\left(\frac{\lambda V_{Li} P_{Li}}{RT}\right) \mathbf{n}_{creep} \tag{3}$$

where j_0 is the flux of the vacancies transporting away from the interface without pressure, in other words, j_0 is equal to $J_{diffusion}$ at the scenario of a non-ideal Li/SE interface with pre-existing defects. λ is the constant which is related to the creep deformation-induced dislocation density of Li metal. V_{Li} is the molar volume of Li metal. R and T are the molar gas constant and temperature respectively. P_{Li} is the hydrostatic pressure in the Li metal. To accurately capture the relationship of the pressure and $\mathbf{J}_{creep}$, $J_{diffusion}$ (or j_0) and λ are calibrated through recent experimentally measured critical stack pressure and the corresponding critical current density, i.e., J_{creep} ($\approx J_{migration}$),[18,22] as shown in Figure 2f. The detailed calibration procedures can be found in Figure S3 (Supporting Information) and the results are listed in Table S1 (Supporting Information). n_{creep} is the direction vector of the creep flow, $\mathbf{n}_{creep} = \nabla \mathbf{P}/|\nabla \mathbf{P}|$. Here, P_{Li} is calculated from our developed creep/contact model, and the creep equation and model details can be found in S1 and Figure S2(Supporting Information).

Figure 2d shows the quantitative analysis and comparison between $J_{migration}$, J_{creep}, and $J_{diffusion}$. It is observed that the calculated J_{creep} is in the range of 0.004 to 0.08 µmol cm^{-2} s^{-1}, when subjected to a stack pressure from 2 to 15 MPa, and it is comparable with the $J_{migration}$, which is between 0.0052 to 0.0363 µmol cm^{-2} s^{-1} when subjected to a current density from 0.5 to 3.5 mA cm^{-2}. $J_{diffusion}$ (whose details can be found in S3, Supporting Information and Figure 2f) is also plotted for reference and its magnitude (0.0025 µmol cm^{-2} s^{-1}) is two orders of magnitude smaller than those for J_{creep} and $J_{migration}$, and thus can be ignored. If $J_{migration}$ is smaller than J_{creep}, e.g., under a high stack pressure or a low stripping current density, J_{creep} is fast enough to move the vacancies away from the interface and into the bulk Li metal. In this case, as a vacancy is generated, J_{creep} is fast enough to move the vacant site into the bulk Li metal before another vacant site is generated. Thus, void formation is suppressed. On the other hand, if $J_{migration}$ is larger than

© 2021 Wiley-VCH GmbH

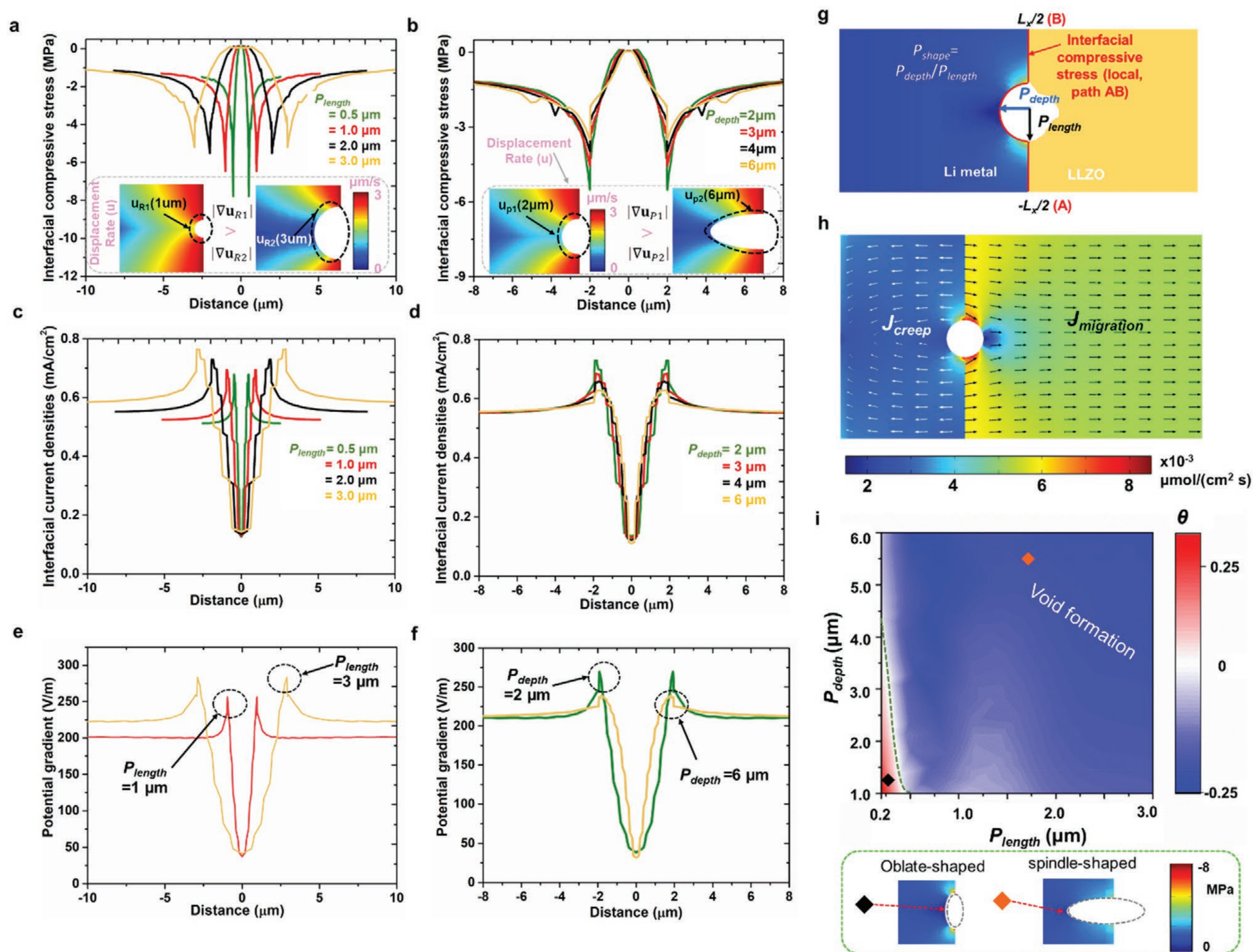

Figure 3. Effect of pre-existing defects on void formation. Distributions of the interfacial compressive stress along the path AB at the Li/SE interface a) at various pore lengths, P_{length} by keeping $P_{depth} = P_{length}$ and b) at different pore depths, P_{depth} by keeping a constant P_{length} (2 µm), where the insert shows the displacement rate for the corresponding cases. Distributions of the interfacial current density along the path AB at c) various P_{length} and d) P_{depth} cases, and the corresponding potential gradient along path AB is shown in (e) and (f) respectively. g) Schematic showing the definition of P_{length}, P_{depth} and path AB. h) The spatial distributions of J_{creep} and $J_{migraiton}$ in a Li/SE system with a pre-existing pore of $P_{length} = P_{depth} = 2$ µm. The direction of $\mathbf{J}_{creep}$ and $\mathbf{J}_{migration}$ are represented by the white and black arrows, respectively. i) A map of void formation as a function of pore length and pore depth. The green dotted line (transition line) shows critical P_{length}/P_{depth} to impede the void formation. Black and orange rhombuses represent the oblate- and spindle-shaped pores respectively.

J_{creep}, e.g., under a small stack pressure or a high stripping current density, the flux of the migrating Li^+ generated-vacancies at the Li/SE interface is higher than the flux of the vacancies transported into the bulk Li metal, and a void will be formed.

2.2.2. Effect of Pre-existing Defect on Void Formation

In this section, comprehensive simulations are performed to illustrate the influence of the pre-existing defect features (e.g., void/pore) on the void formation. The defect parameters, i.e., pore length, P_{length} in the range of 0.2 to 3.0 µm and pore depth, P_{depth} from 1.0 to 6.0 µm, are determined through the reported experimental results,[48] as depicted in **Figure 3**g. A stack pressure of 3 MPa and current density of 0.5 mA cm^{-2} are applied, which are located close to the critical line of the void formation (see Figure S8a in the Supporting Information). The other simulation parameters and boundary/initial conditions can be found in S6 and Figure S6 (Supporting Information). To calculate J_{creep}, we develop a new creep/contact model to calculate the local creep stress distribution of Li metal by presuming that the strain-rate-dependent deformation of Li metal behaves like an incompressible viscous fluid flow. A full description and derivation of this creep/contact model can be found in S1 and Figure S2 (Supporting Information), and the model validation is detailed described in Figure 2e and S3 (Supporting Information).

To illustrate the impact of P_{length} and P_{depth} on the void formation, the compressive stress and current density along the interface in the local region near the pore (i.e., path AB, see Figure 3g) are investigated. Figure 3a,b plots the dependence of the interfacial compressive stress on P_{length} and P_{depth} respectively. It can be observed that the interfacial compressive stress near the pore edges decreases with the increase of P_{length}.

© 2021 Wiley-VCH GmbH

It indicates that J_{creep} decreases with increasing P_{length}. On the other hand, the interfacial compressive stress near the pore edges decreases with increasing P_{depth} as shown in Figure 3b, implying that J_{creep} decreases with increasing P_{depth}. This is probably attributed to the fact that the cases with a smaller P_{length} (see the inset of Figure 3a) or P_{depth} (see the inset of Figure 3b) present a larger gradient of the displacement rate (i.e., strain rate) near the pore edges, which is positively correlated to the creep stress (see creep constitutive: Equations S6 and S7, Supporting Information). In addition, as observed, the interfacial compressive stress is concentrated at the pore edges. One potential reason is that the strain rate near the pore edges is much larger.

Figure 3c,d plots the dependence of the interfacial current density on P_{length} and P_{depth}, respectively. The results show that the interfacial current density near the pore edges increases with the increase of P_{length}. It indicates that $J_{migration}$ increases with increasing P_{length}. While the interfacial current density near the pore edges decreases with the increase of P_{depth}, as shown in Figure 3d, implying that $J_{migration}$ decreases with increasing P_{depth}. One potential reason is that the higher potential gradient is presented for the case with a higher P_{length}, as shown in Figure 3e. On the contrary, the higher P_{depth} leads to the lower potential gradient, as shown in Figure 3f. Note that both J_{creep} and $J_{migration}$ are heterogeneously distributed and concentrated near the pore edges, as shown in Figure 3h. This is probably attributed to the fact that both the interfacial compressive stress and current density are concentrated near the pore edges.

We then introduce θ as a parameter to indicate whether void formation exists on the interface, and it can be expressed as

$$\theta = \log\left(\int_{-L\chi/2}^{L\chi/2} J_{creep}^{local}\, dl / \int_{-L\chi/2}^{L\chi/2} J_{migration}^{local}\, dl \right) \quad (4)$$

where L_x is the local length in the y-direction and the selection of L_χ can be found in S7 and Figure S7a (Supporting Information). For example, if $\theta < 0$, voids are formed and they may cause the contact loss at the Li/SE interface; however, if $\theta > 0$, the initial contact interface is maintained and no void is formed. In addition, as shown in Figure S10 (Supporting Information), if we regard each valley or peak at the surface of SE as an irregular "pore," then, the valley depth or peak height can be regarded as the "$P_{depth,}$" and the width of the valley or peak can be regarded as the "P_{length}." Based on the above, the root-mean square roughness (RMS) and mean width of profile elements (RSm) are, respectively, roughly estimated via pore depth and pore length, i.e., (RMS ≈ P_{depth} and RSm ≈ P_{length}).

Figure 3i represents the map of void formation as a function of P_{length} and P_{depth}. In general, θ increases when the pore is "shallow and narrow." For example, when P_{depth} < 2.5 µm and P_{length} < 0.5 µm, the void formation is impeded. This suggests that the SE surface with a smaller RMS (<2.5 µm) and RSm (<0.5 µm) is favorable. However, when P_{depth} >3.5 µm or P_{length} > 2 µm, the void will be formed at the interface. Hence, a larger RMS (>3.5 µm) or RSm (>2 µm) should be avoided as far as possible. Another interesting observation is that the pre-existing pores with a small length, P_{length} at the interface are desirable, while the influence of the pre-existing pore depth, P_{depth} on void formation is relatively trivial. In other words, the oblate-shaped ($P_{shape} = P_{depth}/P_{length} = 1$) pre-existing pores more effectively impede void growth than the spindle-shaped ($P_{shape} = 3$) pre-existing pores, which may be due to the higher compressive stress near the oblate-shaped pore edges than that of spindle-shaped pores (see Figure 3i bottom).

Therefore, for increasing the interfacial contact during stripping, surface or interface engineering methods should be applied to make the Li/SE interface as flat as possible. For example, nanopolishing (reported by Wang et al.[49]) can be used to effectively reduce the pore/defect length and obtain an ultra-flat surface for solid electrolyte. Surface corrosion and etching can also be applied to modify the surface morphology such as defect shape.[29] Also, other methods, including spin coating,[50] melting lithium,[51,52] interfacial modification,[53] etc. are used to enhance the physical and chemical contact and reduce the influence of the surface of SE.

2.2.3. Effect of Operation Conditions on Void Formation

To determine the effect of stack pressure and current density on the void formation, high-throughput simulations are performed in this section. A current density in the range of 0.1 to 3.5 mA cm^{-2} and a stack pressure from 2 to 15 MPa are carefully chosen based on the reported literature.[17,18,21,29,31,38,45] The other simulation parameters and boundary/initial conditions can be found in S6 and Figure S6 (Supporting Information).

Figure 4a,b shows the dependence of the interfacial compressive stress on stack pressure and current density, respectively. As expected, it can be observed that the interfacial compressive stress and J_{creep} increase with an increase of stack pressure (see Figure 4a). On the other hand, the effect of current density on the interfacial compressive stress and J_{creep} is almost negligible (see Figure 4b). Figure 4c,d plots the dependence of the interfacial current density on stack pressure and current density respectively. Again, as expected, the interfacial current density is almost unchanged with the increase of stack pressure, while the dominator for the interfacial current density and $J_{migration}$ is the applied current density.

To clarify the competition mechanism between vacancy fluxes, the quantities of integral J_{creep} and $J_{migration}$ near the pore edges (i.e., along path AB, see Figure 3g) are compared in Figure 4e, which yields a map of void formation as a function of stack pressure and current density (Figure 4f). The pre-existing pore length, P_{length}, and pore depth, P_{depth}, are set as 2 and 2 µm, respectively. The critical line (green dotted line) represents J_{creep} being equal to $J_{migration}$. Above the line, e.g., under a low stack pressure (<5 MPa), when the applied current density is larger than 0.5 mA cm^{-2}, $J_{migration}$ is larger than J_{creep}, resulting in the formation of voids. While below the line, e.g., under a high stack pressure (>15 MPa), J_{creep} is sufficiently fast to move away from the vacancies, even under the condition of the higher current density (2.0–3.5 mA cm^{-2}). This means that void formation is impeded and the original contact surface is maintained. The experimental results available in the literature[18,22] are also plotted in Figure 4f, and a general consistency is observed.

Figure 4g further explores the impact of pre-existing pore length P_{length} (from 1 to 3 µm) on the map of void formation. It is observed that the critical line of the map of void formation

 © 2021 Wiley-VCH GmbH

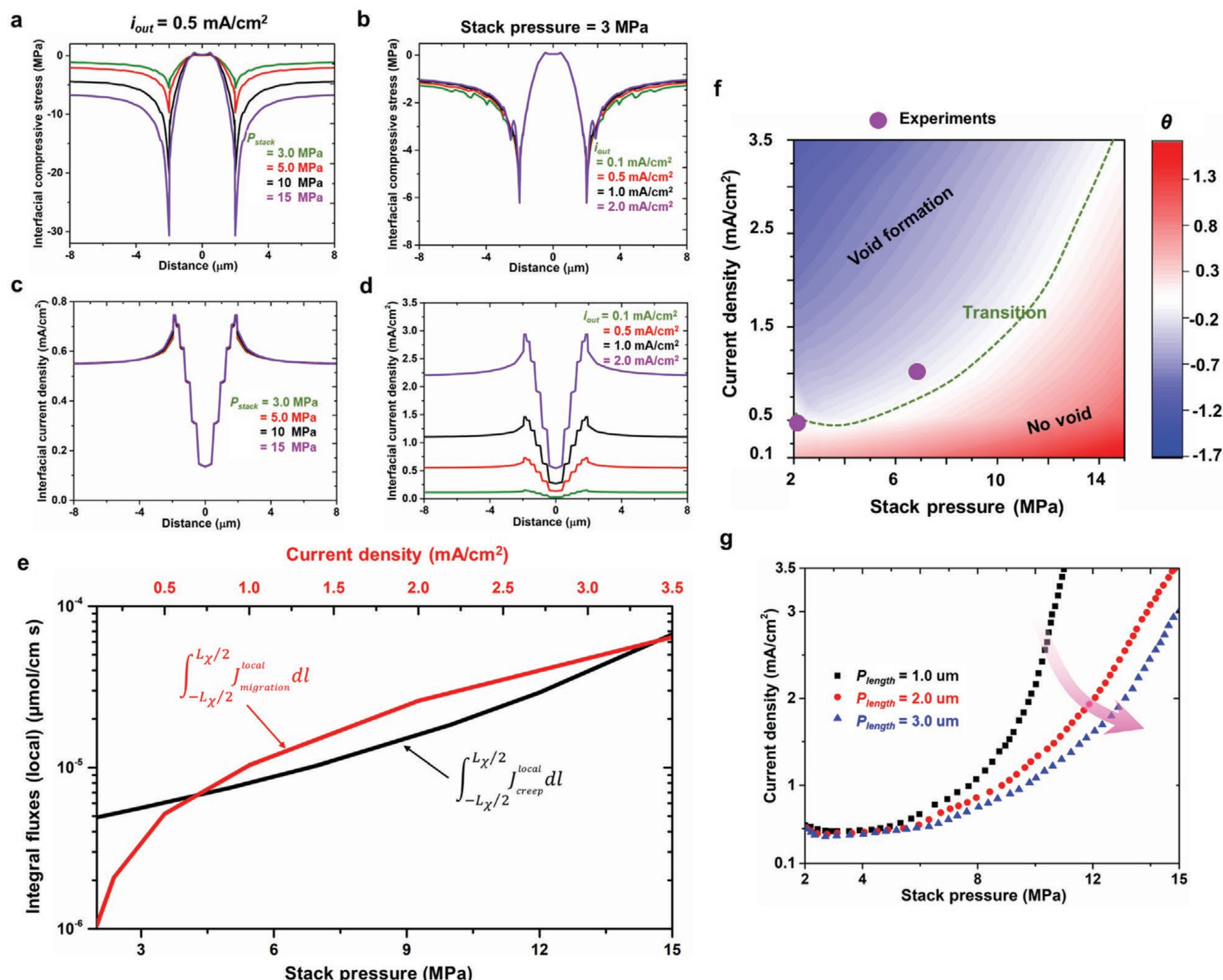

Figure 4. Effect of operation conditions on void formation. Distributions of the interfacial compressive stress along the path AB (see Figure 3g) at the Li/SE interface at a) various stack pressures subjected to a current density of 0.5 mA cm^{-2}, and b) various current densities subjected to a stack pressure of 3 MPa. The corresponding distributions of the interfacial current density are plotted in c) and d) respectively. e) Comparison between the integral of J_{creep} (i.e., $\int_{-L\chi/2}^{L\chi/2} J_{creep}^{local}\,dl$) and $J_{migration}$ (i.e., $\int_{-L\chi/2}^{L\chi/2} J_{migration}^{local}\,dl$) near the pore edges. f) A map of void formation as a function of stack pressure and current density. The green dotted line (transition line) shows critical stack pressure/current density for void formation. The purple circles represent the experimental reported results.[18,22] g) Impact of pre-existing pore length P_{length} on the map of void formation.

is shifted down with the increase of P_{length}. It means that at the same conditions, the higher stack pressure or lower current density is necessary to impede void formation under a larger P_{length}. One potential reason is that the larger P_{length} presents a smaller interfacial compressive stress which is positively correlated to the J_{creep} (see Equation (3)).

The map of void formation can inform whether the stack pressure sufficiently impedes void formation under realistic experimental operations. For example, the practical application of next-generation SSBs[45,54] requires a current density higher than 2.5 mA cm^{-2}. Thus, according to our map, the stack pressure should be larger than 12 MPa to impede the void formation, which is approximately observed in the experimental results.[55] However, a recent experiment shows that a very high stack pressure (75 MPa) leads to the mechanical shorting of the cell before any plating and stripping.[21] Therefore, the reasonable range of stack pressure to completely impede the void formation is from 12 to 75 MPa. In addition, high stack pressure (>10 MPa) is achieved in some experimental works;[21,56] however, for commercial-size battery (e.g., pouch cell), the application of high stack pressure remains a challenge.

2.2.4. Interface Mechanical Stability Window for Different Li-SE Systems

To screen the SE systems with better interfacial mechanical stability, the effect of material properties (i.e., ionic conductivity and exchange current density) of SEs on the void formation behavior is extensively investigated. The stack pressure of 3 MPa and current density of 0.5 mA cm^{-2} (which are commonly used in experiments[17,18,22]) are applied with pore

© 2021 Wiley-VCH GmbH

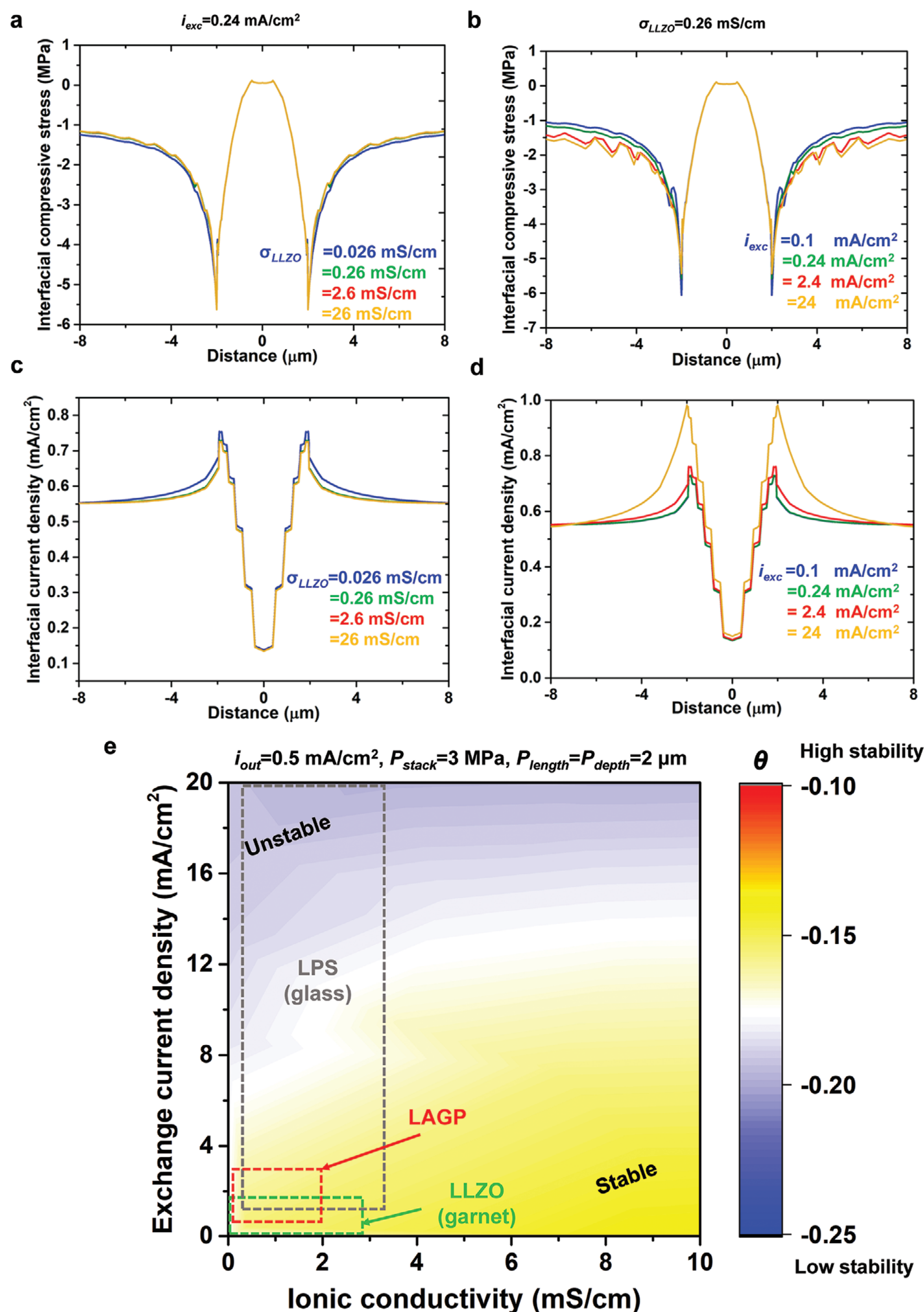

Figure 5. Interface mechanical stability window for different Li-SE systems. Distributions of the interfacial compressive stress along the path AB at the Li/SE interface at a) various ionic conductivities with an exchange current density of 0.24 mA cm^{-2}, and b) different exchange current densities with a constant ionic conductivity of 0.26 mS cm^{-1}. The corresponding distributions of the interfacial current density are plotted in c,d) respectively. e) The interface mechanical stability window against ionic conductivity and exchange current density for different Li-SE systems, with stack pressure of 3 MPa and current density of 0.5 mA cm^{-2} and P_{length} = P_{depth} = 2 µm. The dotted rectangles represent the typical range of ionic conductivity and exchange current density for different SEs.

size P_{length} = P_{depth} = 2 µm. A typical range of the ionic conductivity (from 10^{-6} to 10^{-2} S cm^{-1})[57] and exchange current density (from 10^{-2} to 10^{2} mA cm^{-2})[58–60] are considered in this study. The other simulation parameters and boundary/initial conditions can be found in S6 and Figure S6 (Supporting Information).

Figure 5a,b shows the dependence of the interfacial compressive stress on ionic conductivity and exchange current density, respectively. It can be observed that the effect of the ionic conductivity on the interfacial compressive stress and J_{creep} is almost negligible (see Figure 5a). On the other hand,

 © 2021 Wiley-VCH GmbH

the interfacial compressive stress near the pore edges increases with the increase of exchange current density (see Figure 5b), implying that J_{creep} increases with increasing exchange current density. Figure 5c,d plots the dependence of the interfacial current density on ionic conductivity and exchange current density, respectively. As expected, it can be observed that the interfacial current density and $J_{migration}$ decrease with the increase of the ionic conductivity (see Figure 5c), while they increase with the increase of the exchange current density (see Figure 5d), both of which are well-supported by recently reported work.[29]

To clarify the effect of the ionic conductivity and exchange current density on interfacial mechanical stability, the quantities of integral J_{creep} and $J_{migration}$ near the pore edges (i.e., along path AB, see Figure 3g) are computed. The comparison of them yields a map of interfacial mechanical stability (θ) for different Li-SE systems as a function of ionic conductivity and exchange current density (Figure 5e). The dotted rectangles represent the typical range of ionic conductivity and exchange current density for different SEs, e.g., LPS (ionic conductivity[57,61,62] from $\approx 10^{-5}$ to $\approx 10^{-3}$ mS cm^{-1} and exchange current density[60,61] from ≈ 0.2 to 20 mA cm^{-2}) and LLZO (ionic conductivity[57,63,64] from $\approx 10^{-5}$ to $\approx 10^{-3}$ mS cm^{-1} and exchange current density[58,64] from 0.04 to ≈ 1 mA cm^{-2}). The yellow and blue colors represent the high or low mechanical stability of the interface, respectively. If the dotted rectangle falls in the blue or white region, e.g., with a high exchange current (>10 mA cm^{-2}) and low ionic conductivity (<0.1 mS cm^{-1}), $J_{migration}$ is much larger than J_{creep}, resulting in a lower interfacial mechanical stability. While if it falls in the yellow region, e.g., with a low exchange current density (<5 mA cm^{-2}) and high ionic conductivity (>1.0 mS cm^{-1}), J_{creep} is close to the $J_{migration}$, implying a high interfacial mechanical stability. This means that $J_{creep} > J_{migration}$ is easily achieved.

This window could give quantitative information on whether the fabricated SE is prone to maintain a more stable interface, and what are the SE's ideal material properties. For example, the major part of the dotted rectangle of the LPS (glass-type) falls in the blue or white-colored region, indicating that it possesses lower interfacial mechanical stability. While LLZO (garnet-type) falls in the yellow-colored region and shows the potential to provide high interfacial stability compared to LPS, which is consistent with observations in the literature.[29,65] Furthermore, the map could also shed insight on the fabrication of the SEs with high interfacial mechanical stability to mitigate the void formation.

2.3. Insights in Void Evolution and Subsequent Plating

Figure 6 demonstrates insights into pore/void evolution and subsequent plating. On the one hand, if $J_{creep} < J_{migration}$, the pre-existing pore will grow, see Figure 6a,b. The red arrows represent the direction of pore growth, and their length represents the rate of the pore growth, which can be quantified as J_{total} where $J_{total} = J_{migration} + J_{creep}$. It can be found that the closer to the middle region of the pore, the shorter the length of the arrow, which can be explained by the fact that closer to the middle region, J_{total} is smaller, as shown in Figure S9 (Supporting Information). J_{total} is accentuated at the edge region of the pre-existing pore, thus, the pore grows along the Li/SE interface. In other words, the pore grows faster in the direction of the pore length compared to the direction of pore depth, which is consistent with experimental observations.[18,55] To quantify the pore growth, we introduce the ratio: P_{length}/P_{depth}, as defined in Figure 6e. The calculated value of P_{length}/P_{depth} is 4.2, when the current density is 1.0 mA cm^{-2} and stack pressure is 3 MPa. Figure 6e also presents the experimental results of the P_{length}/P_{depth} after stripping cycles,[18,55] which shows excellent agreement with our predictions. Moreover, for the subsequent plating, the current density is enhanced at the edge region of the pore, implying a large amount of Li^+ moving for Li deposition. Thus, the dendrite nucleates at the edges of the pore as shown in Figure 6c.

On the other hand, once $J_{creep} > J_{migration}$, J_{total} tends to move the vacancies away from the interface and towards the bulk Li metal, as shown in Figure 6d. Thus, there are no vacancies left at the interface, and consequently, pore growth is suppressed. When $J_{creep} >> J_{migration}$, with respect to the creep deformation of Li metal, we speculate that the vacancy flux could reduce the volume of the pre-existing pore and even annihilate the pore, along the direction of the red arrows. This can be explained by the fact that the Li atoms occupy the sites of the vacancies near pre-existing pore, especially along the direction of the edge region near the pore due to the electro-chemo-mechanical interplay at the interface.

3. Conclusion

In summary, we have developed a new general creep/contact electro-chemo-mechanical model to reveal the mechanisms of void formation during stripping. The creep-stress evolution of Li metal is calculated by introducing a novel FSI theory where the creep deformation is analogous to the incompressible viscous fluid flow. First, a 1D model with the ideal flat Li/SE interface is formulated out to clarify the competition between $J_{diffusion}$ and $J_{migration}$ during void formation. Meanwhile, for the non-ideal Li/SE interface, the effects of pre-existing defect features (e.g., pore length and pore depth) on the void formation are comprehensively investigated. Our results demonstrate that the dominant mechanism to impede void formation is the creep-induced flux enhancement of vacancies transported into Li metal for a non-ideal Li/SE interface with pre-existing defects, which contrasts with the mechanism on the ideal flat Li/SE interface in which the vacancy diffusion away from the interface governs whether a void is formed.

Then, to determine the preferred stack pressure that could impede the void formation under different requirements, we further explore the competitive influences between stack pressure and current density on void formation at the non-ideal Li/SE interface with pre-existing defects, yielding a map that can inform whether the stack pressure sufficiently impedes the void formation. The map suggests that the preferred stack pressure should be higher than 12 MPa to maintain relatively intimate interfacial contact at a widely used current density (e.g., 2–3 mA cm^{-2}). Further, we found that the pre-existing pore size can shift downward the critical line in the map of void formation.

Lastly, we perform high-throughput simulations to draw an interfacial mechanical stability window that provides

© 2021 Wiley-VCH GmbH

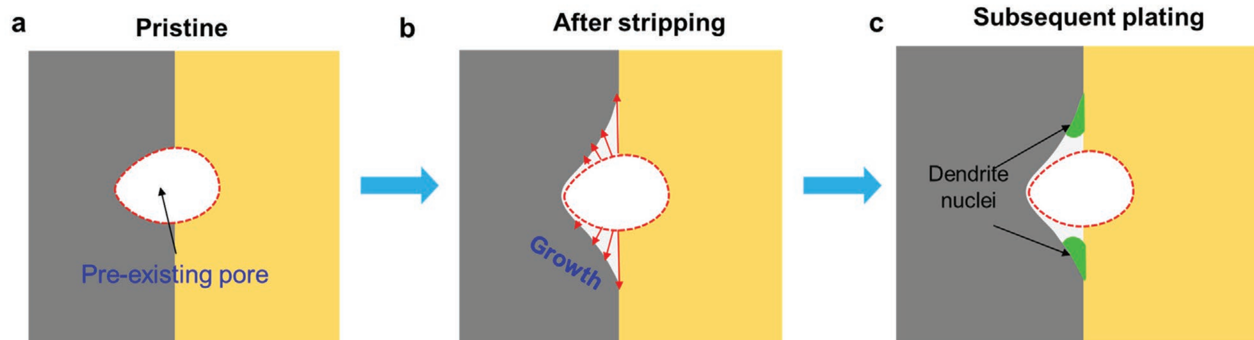

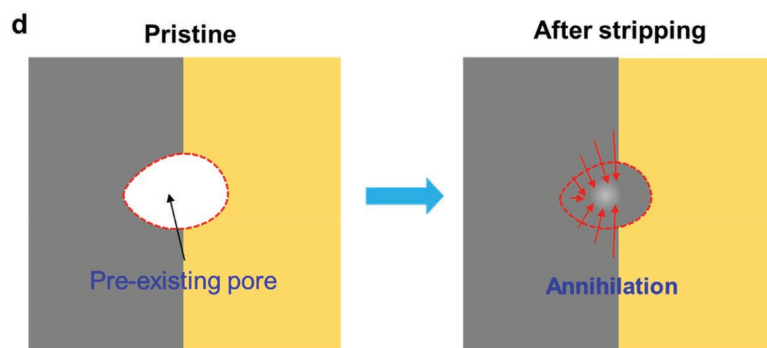

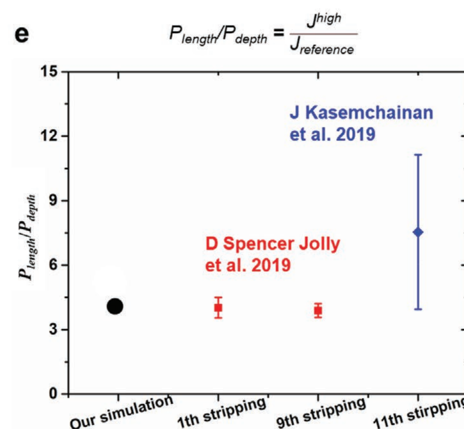

Figure 6. Insights of the pore evolution and subsequent plating. a) Schematic diagram of the initial interfacial geometry between Li metal and SE. b) When $J_{creep} < J_{migration}$, the tendency of the pore growth is described by the direction and length of the red arrows. c) On subsequent plating, the Li dendrite nucleates at the edges of the pore. d) Schematic diagram of the pore annihilation. e) The comparison of the calculated P_{length}/P_{depth} for the case of pore growth with the reported P_{length}/P_{depth} in literatures, Jolly et al.[55] and Kasemchainan et al.[18]

quantitative information on how the interplay between ionic conductivity and exchange current density influence the Li/SE interfacial mechanical stability. The window can give an idea of what intrinsic SE properties might lead to high interfacial mechanical stability as well as what type of SEs (e.g., LLZO) might present a more stable interface. Further experiments can be feasibly designed to verify this approach. We hope this fundamental and quantitative understanding of the void formation mechanism will help accelerate the rational design of SSBs.

Supporting Information

Supporting Information is available from the Wiley Online Library or from the author.

Acknowledgements

This work was financially supported by National Natural Science Foundation of China (11872177) and Ford Summer Sabbatical Program. K.T. and L.C. greatly appreciate the startup funding from UM-Dearborn. H.H.Y. greatly appreciates the China Scholarship Council. The authors acknowledge Professor Yue Qi for valuable discussions about this work.

Conflict of Interest

The authors declare no conflict of interest.

Data Availability Statement

Research data are not shared.

Keywords

creep/contact model, interfacial contact, Li anodes, Li stress, solid-state batteries, void formation

Received: July 26, 2021
Revised: October 14, 2021
Published online: November 10, 2021

[1] F. Zheng, M. Kotobuki, S. Song, M. O. Lai, L. Lu, *J. Power Sources* **2018**, *389*, 198.
[2] K. Takada, *J. Power Sources* **2018**, *394*, 74.
[3] C. Monroe, J. Newman, *J. Electrochem. Soc.* **2005**, *152*, A396.
[4] D. Cao, X. Sun, Q. Li, A. Natan, P. Xiang, H. Zhu, *Matter* **2020**, *3*, 57.

© 2021 Wiley-VCH GmbH

[5] E. Kazyak, R. Garcia-Mendez, W. S. LePage, A. Sharafi, A. L. Davis, A. J. Sanchez, K. H. Chen, C. Haslam, J. Sakamoto, N. P. Dasgupta, *Matter* **2020**, *2*, 1025.
[6] A. S. Westover, N. J. Dudney, R. L. Sacci, S. Kalnaus, *ACS Energy Lett.* **2019**, *4*, 651.
[7] E. J. Cheng, A. Sharafi, J. Sakamoto, *Electrochim. Acta* **2017**, *223*, 85.
[8] R. H. Basappa, T. Ito, H. Yamada, *J. Electrochem. Soc.* **2017**, *164*, A666.
[9] H. Koshikawa, S. Matsuda, K. Kamiya, M. Miyayama, Y. Kubo, K. Uosaki, K. Hashimoto, S. Nakanishi, *J. Power Sources* **2018**, *376*, 147.
[10] M. Botros, R. Djenadic, O. Clemens, M. Möller, H. Hahn, *J. Power Sources* **2016**, *309*, 108.
[11] J. Wen, Y. Huang, J. Duan, Y. Wu, W. Luo, L. Zhou, C. Hu, L. Huang, X. Zheng, W. Yang, Z. Wen, Y. Huang, *ACS Nano* **2019**, *13*, 14549.
[12] J. Duan, L. Huang, T. Wang, Y. Huang, H. Fu, W. Wu, W. Luo, Y. Huang, *Adv. Funct. Mater.* **2020**, *30*, 1908701.
[13] T. Shi, Y. Q. Zhang, Q. Tu, Y. Wang, M. C. Scott, G. Ceder, *J. Mater. Chem. A* **2020**, *8*, 17399.
[14] J. A. Lewis, F. J. Q. Cortes, Y. Liu, J. C. Miers, A. Verma, B. S. Vishnugopi, J. Tippens, D. Prakash, T. S. Marchese, S. Y. Han, C. Lee, P. P. Shetty, H. W. Lee, P. Shevchenko, F. De Carlo, C. Saldana, P. P. Mukherjee, M. T. McDowell, *Nat. Mater.* **2021**, *20*, 503.
[15] S. Lou, Q. Liu, F. Zhang, Q. Liu, Z. Yu, T. Mu, Y. Zhao, J. Borovilas, Y. Chen, M. Ge, X. Xiao, W. K. Lee, G. Yin, Y. Yang, X. Sun, J. Wang, *Nat. Commun.* **2020**, *11*, 57.
[16] A. C. Luntz, J. Voss, K. Reuter, *J. Phys. Chem. Lett.* **2015**, *6*, 4599.
[17] Y. Wang, T. Liu, J. Kumar, *ACS Appl. Mater. Interfaces* **2020**, *12*, 34771.
[18] J. Kasemchainan, S. Zekoll, D. S. Jolly, Z. Ning, G. O. Hartley, J. Marrow, P. G. Bruce, *Nat. Mater.* **2019**, *18*, 1105.
[19] T. Krauskopf, H. Hartmann, W. G. Zeier, J. Janek, *ACS Appl. Mater. Interfaces* **2019**, *11*, 14463.
[20] X. Zhang, Q. Xiang, S. Tang, A. Wang, X. Liu, J. Luo, *Nano Lett.* **2020**, *20*, 2871.
[21] J. M. Doux, H. Nguyen, D. H. S. Tan, A. Banerjee, X. Wang, E. A. Wu, C. Jo, H. Yang, Y. S. Meng, *Adv. Energy Mater.* **2020**, *10*, 1903253.
[22] M. J. Wang, R. Choudhury, J. Sakamoto, *Joule* **2019**, *3*, 2165.
[23] C.-T. Yang, Y. Qi, *Chem. Mater.* **2021**, *33*, 2814.
[24] L. Porz, T. Swamy, B. W. Sheldon, D. Rettenwander, T. Frömling, H. L. Thaman, S. Berendts, R. Uecker, W. C. Carter, Y. M. Chiang, *Adv. Energy Mater.* **2017**, *7*, 1701003.
[25] K. Lu, C. F. Huo, Y. He, J. Yin, J. Liu, Q. Peng, W. P. Guo, Y. Yang, Y. W. Li, X. D. Wen, *J. Phys. Chem. C* **2018**, *122*, 23191.
[26] F. Zhang, A. M. Walker, K. Wright, J. D. Gale, *J. Mater. Chem.* **2010**, *20*, 10445.
[27] L. Zhang, T. Yang, C. Du, Q. Liu, Y. Tang, J. Zhao, B. Wang, T. Chen, Y. Sun, P. Jia, H. Li, L. Geng, J. Chen, H. Ye, Z. Wang, Y. Li, H. Sun, X. Li, Q. Dai, Y. Tang, Q. Peng, T. Shen, S. Zhang, T. Zhu, J. Huang, *Nat. Nanotechnol.* **2020**, *15*, 94.
[28] Y. Chen, Z. Wang, X. Li, X. Yao, C. Wang, Y. Li, W. Xue, D. Yu, S. Y. Kim, F. Yang, A. Kushima, G. Zhang, H. Huang, N. Wu, Y. W. Mai, J. B. Goodenough, J. Li, *Nature* **2020**, *578*, 251.
[29] Q. Tu, L. Barroso-Luque, T. Shi, G. Ceder, *Cell Rep. Phys. Sci.* **2020**, *1*, 100106.
[30] Y. He, X. Ren, Y. Xu, M. H. Engelhard, X. Li, J. Xiao, J. Liu, J. G. Zhang, W. Xu, C. Wang, *Nat. Nanotechnol.* **2019**, *14*, 1042.
[31] X. Zhang, Q. J. Wang, K. L. Harrison, S. A. Roberts, S. J. Harris, *Cell Rep. Phys. Sci.* **2020**, *1*, 100012.
[32] W. S. LePage, Y. Chen, E. Kazyak, K. H. Chen, A. J. Sanchez, A. Poli, E. M. Arruda, M. D. Thouless, N. P. Dasgupta, *J. Electrochem. Soc.* **2019**, *166*, A89 .
[33] A. Masias, N. Felten, R. Garcia-Mendez, J. Wolfenstine, J. Sakamoto, *J. Mater. Sci.* **2019**, *54*, 2585.
[34] C. D. Fincher, D. Ojeda, Y. Zhang, G. M. Pharr, M. Pharr, *Acta Mater.* **2020**, *186*, 215.
[35] J. Wolfenstine, J. L. Allen, J. Sakamoto, D. J. Siegel, H. Choe, *Ionics* **2018**, *24*, 1271.
[36] M. Wang, J. B. Wolfenstine, J. Sakamoto, *Electrochim. Acta* **2019**, *296*, 842
[37] H. Schmalzried, J. Janek, *Ber. Bunsengesellschaft/Phys. Chem. Chem. Phys.* **1998**, *102*, 127.
[38] F. Shi, A. Pei, D. T. Boyle, J. Xie, X. Yu, X. Zhang, Y. Cui, *Proc. Natl. Acad. Sci. USA* **2018**, *115*, 8529.
[39] M. Yang, Y. Liu, A. M. Nolan, Y. Mo, *Adv. Mater.* **2021**, *33*, 2008081.
[40] Y. T. Chiu, K. L. Lin, Y. S. Lai, *J. Appl. Phys.* **2012**, *111*, 043517.
[41] W. Frank, U. Breier, C. Elsässer, M. Fähnle, *Phys. Rev. Lett.* **1996**, *77*, 518.
[42] T. R. Jow, C. C. Liang, *J. Electrochem. Soc.* **1983**, *130*, 737.
[43] R. Messer, F. Noack, *Appl. Phys.* **1975**, *6*, 79.
[44] E. Dologlou, *Glass Phys. Chem.* **2010**, *36*, 570.
[45] P. Albertus, S. Babinec, S. Litzelman, A. Newman, *Nat. Energy* **2018**, *3*, 16.
[46] M. Jäckle, K. Helmbrecht, M. Smits, D. Stottmeister, A. Groß, *Energy Environ. Sci.* **2018**, *11*, 3400.
[47] K. Yoshimi, M. Tsunekane, R. Nakamura, A. Yamauchi, S. Hanada, *Appl. Phys. Lett.* **2006**, *89*, 073110.
[48] F. Shen, M. B. Dixit, X. Xiao, K. B. Hatzell, *ACS Energy Lett.* **2018**, *3*, 1056.
[49] S. Wang, J. Wang, J. Liu, H. Song, Y. Liu, P. Wang, P. He, J. Xu, H. Zhou, *J. Mater. Chem. A* **2018**, *6*, 21248.
[50] Z. Zhang, S. Chen, J. Yang, J. Wang, L. Yao, X. Yao, P. Cui, X. Xu, *ACS Appl. Mater. Interfaces* **2018**, *10*, 2556.
[51] Y. Ruan, Y. Lu, X. Huang, J. Su, C. Sun, J. Jin, Z. Wen, *J. Mater. Chem. A* **2019**, *7*, 14565.
[52] M. Cai, Y. Lu, L. Yao, J. Jin, Z. Wen, *Chem. Eng. J.* **2021**, *417*, 129158.
[53] W. Li, Q. Wang, J. Jin, Y. Li, M. Wu, Z. Wen, *Energy Storage Mater.* **2019**, *23*, 299.
[54] F. Flatscher, M. Philipp, S. Ganschow, H. M. R. Wilkening, D. Rettenwander, *J. Mater. Chem. A* **2020**, *8*, 15782.
[55] D. S. Jolly, Z. Ning, J. E. Darnbrough, J. Kasemchainan, G. O. Hartley, P. Adamson, D. E. J. Armstrong, J. Marrow, P. G. Bruce, *ACS Appl. Mater. Interfaces* **2020**, *12*, 678.
[56] C. Lee, S. Y. Han, J. A. Lewis, P. P. Shetty, D. Yeh, Y. Liu, E. Klein, H. W. Lee, M. T. McDowell, *ACS Energy Lett.* **2021**, *6*, 3261.
[57] J. C. Bachman, S. Muy, A. Grimaud, H. H. Chang, N. Pour, S. F. Lux, O. Paschos, F. Maglia, S. Lupart, P. Lamp, L. Giordano, Y. Shao-Horn, *Chem. Rev.* **2016**, *116*, 140.
[58] P. Barai, A. T. Ngo, B. Narayanan, K. Higa, L. A. Curtiss, V. Srinivasan, *J. Electrochem. Soc.* **2020**, *167*, 100537.
[59] M. Schleutker, J. Bahner, C. L. Tsai, D. Stolten, C. Korte, *Phys. Chem. Chem. Phys.* **2017**, *19*, 26596.
[60] M. Chiku, W. Tsujiwaki, E. Higuchi, H. Inoue, *Electrochemistry* **2012**, *80*, 740
[61] T. Yamada, S. Ito, R. Omoda, T. Watanabe, Y. Aihara, M. Agostini, U. Ulissi, J. Hassoun, B. Scrosati, *J. Electrochem. Soc.* **2015**, *162*, A646.
[62] R. Garcia-Mendez, F. Mizuno, R. Zhang, T. S. Arthur, J. Sakamoto, *Electrochim. Acta* **2017**, *237*, 144.
[63] Z. Ding, J. Li, J. Li, C. An, *J. Electrochem. Soc.* **2020**, *167*, 070541.
[64] H. Buschmann, S. Berendts, B. Mogwitz, J. Janek, *J. Power Sources* **2012**, *206*, 236.
[65] Y. Xiao, Y. Wang, S. H. Bo, J. C. Kim, L. J. Miara, G. Ceder, *Nat. Rev. Mater.* **2020**, *5*, 105.

© 2021 Wiley-VCH GmbH